

# Optical coupling optimization in a novel metal–semiconductor–metal ultraviolet photodetector based on semicircular Schottky electrodes\*

Chen Bin(陈斌)<sup>1, †</sup>, Yang Yintang(杨银堂)<sup>1</sup>, Chai Changchun(柴常春)<sup>1</sup>, Wang Ning(王宁)<sup>1</sup>,  
Ma Zhenyang(马振洋)<sup>1</sup>, and Xie Xuanrong(谢宣蓉)<sup>2</sup>

<sup>1</sup>Key Laboratory of Ministry of Education for Wide Band-Gap Semiconductor Materials and Devices,  
School of Microelectronics, Xidian University, Xi'an 710071, China

<sup>2</sup>No.771 Institute of Microelectronics Technology, Xi'an 710054, China

**Abstract:** A novel semicircular electrode metal–semiconductor–metal (SEMSM) ultraviolet detector is modeled, investigated and characterized with a self-consistent numerical calculation method. For the purpose of model and performance verification, a comprehensive comparison of the SEMSM detector and a conventional electrode MSM detector is carried out with experimental data. The results indicate that the physical models are able to predict the enhanced device features. Moreover, the structural parameters have been adjusted appropriately to optimize the SEMSM detector. The findings show that a device with a 2  $\mu\text{m}$  finger radius and 3  $\mu\text{m}$  spacing exhibits outstanding characteristics in terms of a peak responsivity of 0.177 A/W at 290 nm, a maximum external quantum efficiency of over 75%, and a comparable normalized photocurrent to dark current ratio of  $1.192 \times 10^{11} \text{ W}^{-1}$  at 0.3 V bias. These results demonstrate that the SEMSM detector has excellent performance for optoelectronic integrated circuit applications.

**Key words:** semicircular contact; MSM ultraviolet photodetector; optimization

**DOI:** 10.1088/1674-4926/33/5/054010

**PACC:** 0670D; 0762; 7820

## 1. Introduction

Since the remarkable progress in the growth and processing of wide bandgap semiconductor materials, photodetectors fabricated with these materials have been recognized as attractive optoelectronic devices for ultraviolet (UV) detection due to their extensive commercial and military applications. In particular, these photodetectors can be used in flame detection, optical communication, emitter calibration, chemical/biological analysis and astronomical studies<sup>[1]</sup>. Though GaN-based UV detectors have the benefit of tunable spectral response and the potential for solar-blindness, their high dislocation densities have limited their performance<sup>[2, 3]</sup>. Owing to the excellent physical property of high breakdown field and high thermal stability, 4H-SiC-based photodetectors are regarded as promising candidates for UV detection under harsh and high-temperature conditions. To date, various types of UV photodetectors have been developed<sup>[4–6]</sup>. In particular, the metal–semiconductor–metal (MSM) structure may be superior due to its large bandwidth, low intrinsic capacitance and easy integration with field effect transistors. Unfortunately, MSM photodetectors still suffer from low responsivity and quantum efficiency due to the optical losses on their opaque metal electrodes. In aiming to conquer these defects, tremendous efforts have been devoted to improve performance, such as utilizing transparent indium tin oxide or nano-grating-assisted structures to form patterns<sup>[7, 8]</sup>, and adopting an integrated microlens array and  $\text{Al}_2\text{O}_3/\text{SiO}_2$  film as antireflection coatings<sup>[9, 10]</sup>. However, these attempts can also cause confusions

and concerns about the physical and mechanical properties, and thermal stability of the contact. Inspiringly, the oval- and circular-shaped contacts in 4H-SiC rectifiers with a junction termination extension have been successfully fabricated<sup>[11]</sup>. From a technical point of view, to adopt semicircular electrodes as Schottky contacts in MSM photodetectors for performance enhancement is feasible. Previously, the concept of the semicircular electrode metal–semiconductor–metal (SEMSM) detector has been proposed<sup>[12]</sup>, however, thoroughly quantitative modeling and analysis are still lacking, and this is not beneficial for the design and optimization of the photodetector.

In this paper, we establish a two-dimensional (2D) model of 4H-SiC-based SEMSM and conventional electrode MSM (CEMSM) detectors using a self-consistent numerical calculation method. By comparing the calculated results and relevant experimental data, the approach used in our study has been verified. The SEMSM detector was then optimized and characterized to obtain the improved performance.

## 2. Methodology

### 2.1. Device design and characterization

In our calculation, the structures of an SEMSM detector and a conventional one are illustrated in Figs. 1(a) and 1(b), respectively. The SEMSM detector consists of a 400  $\mu\text{m}$ -thick n-type 4H-SiC substrate and a 5  $\mu\text{m}$ -thick epitaxial layer with doping concentrations of  $10^{20} \text{ cm}^{-3}$  and  $9 \times 10^{15} \text{ cm}^{-3}$ . In order to form a planar interdigital structure, semicircular Au

\* Project supported by the Pre-Research Foundation from the National Ministries and Commissions of China (Nos. 51323040118, 513080302).

† Corresponding author. Email: xidianchenbin@163.com

Received 17 October 2011, revised manuscript received 14 December 2011

© 2012 Chinese Institute of Electronics

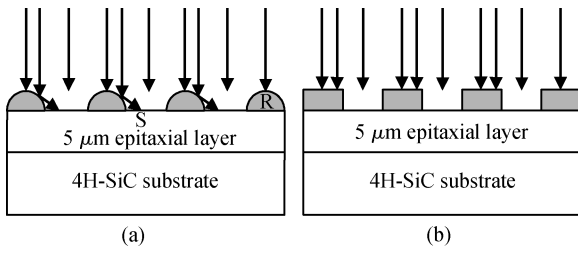


Fig. 1. Schematic diagram of (a) a semicircular electrode MSM photodetector and (b) a conventional structure.

Table 1. The simulation model parameters assumed at room temperature<sup>[16, 21, 22]</sup>.

Parameter	Value
Beta0	1.23
Bataexp	0.17
$E_g$	3.26 eV
$E_{g0}$	3.359 eV
Alpha	$3.3 \times 10^{-4}$ eV/K
Beta	0 K
$E_{ND}$	0.065 eV
Alpha_N	$3.1 \times 10^{-8}$ eV·cm
$g_{ND}$	2
Xsec_N	$1 \times 10^{-12}$ cm <sup>2</sup> /s
NdCrit	$1 \times 10^{22}$ cm <sup>-3</sup>
$C_n$	$5 \times 10^{-31}$ cm <sup>6</sup> /s
$C_p$	$2 \times 10^{-31}$ cm <sup>6</sup> /s
Diffusion coefficient	3.4 cm <sup>2</sup> /s
Lifetime $\tau$	11 ns
Diffusion length	1.934 $\mu$ m

Schottky contact electrodes with a radius of 1.5  $\mu$ m are employed on top of the epitaxial layer, forming the anode and the cathode. The fingers are 3  $\mu$ m wide and 500  $\mu$ m long with a spacing of 3  $\mu$ m. The optically sensitive area is 200  $\times$  500  $\mu$ m<sup>2</sup>. In contrast, as illustrated in Fig. 1(b), the same structural CEMSM UV detector but with different 80 nm-thick conventional electrodes is also calculated, similar to the realistic detector previously reported in Ref. [13].

## 2.2. Physical and material models

To investigate and predict the electrical and optical characteristics of the novel photodetector, the commercially available Integrated Systems Engineering DESSIS is adopted to solve Poisson's equation, the current continuity equation and the current density equation based on a series of physical models, including Shockley–Read–Hall, for generation and recombination; the thermionic emission model for a description of the heterojunction interface between the metal and the semiconductor; the barrier lowering model for interpreting the effects of image force barrier lowering; and the photo-generation rate model for determining the optical characteristics of the device. In addition, we set the incidence optical power as 0.25  $\mu$ W, and the wavelength dependent absorption coefficients are obtained in Ref. [14]. The electrode reflection coefficient is calculated from Ref. [15]. A more detailed description of the above models can be specified in Ref. [16], and similar modeling and simulation methods are presented elsewhere<sup>[17]</sup>. Here, we elab-

orate on the models accounting for mobility, ionization and recombination. The detailed model and material parameters of 4H-SiC are summarized in Table 1.

The high field dependent mobility model originates from the Caughey–Thomas formula.

$$\mu(F) = \frac{\mu_{low}}{\left[1 + \left(\frac{\mu_{low}F}{v_{sat}}\right)^\beta\right]^{1/\beta}}, \quad (1)$$

$$\beta = \beta_0 \left(\frac{T}{T_0}\right)^{\beta_{exp}}, \quad (2)$$

where  $\mu_{low}$  denotes the low field mobility. The exponent  $\beta$  is the temperature-dependent factor.

The temperature dependence of the band gap is described as:

$$E_g(t) = E_g(0) - \frac{\alpha t^2}{t + \beta}. \quad (3)$$

The concentration of ionized impurity is given by Fermi–Dirac distribution. Incomplete ionization in the SiC material has been considered. The corresponding distribution function can be expressed as<sup>[18]</sup>:

$$N_D^+ = \frac{N_D}{1 + G_D(T) \exp\left(\frac{E_{F_n} - E_C}{K_B T}\right)}, \quad (4)$$

$$N_A^- = \frac{N_A}{1 + G_A(T) \exp\left(\frac{E_{F_p} - E_V}{K_B T}\right)}, \quad (5)$$

where  $G_D(T)$  and  $G_A(T)$  are the ionization factors discussed in Refs. [19, 20], which is given by:

$$G_D(T) = g_D \exp\left(\frac{\Delta E_D}{K_B T}\right), \quad \Delta E_D = E_C - E_D, \quad (6)$$

$$G_A(T) = g_A \exp\left(\frac{\Delta E_A}{K_B T}\right), \quad \Delta E_A = E_A - E_V. \quad (7)$$

With the coefficient  $C_n$  and  $C_p$  obtained in Ref. [21]. The Auger recombination mechanism is also invoked in our calculation by means of

$$R^A = (C_n n + C_p p)(np - n_{i,eff}^2), \quad (8)$$

$$C_n(T) = \left[A_{A,n} + B_{A,n} \frac{T}{T_0} + C_{A,n} \left(\frac{T}{T_0}\right)^2\right] \left(1 + H_n e^{-\frac{n}{N_{0,n}}}\right), \quad (9)$$

$$C_p(T) = \left[A_{A,p} + B_{A,p} \frac{T}{T_0} + C_{A,p} \left(\frac{T}{T_0}\right)^2\right] \left(1 + H_p e^{-\frac{p}{N_{0,p}}}\right), \quad (10)$$

where  $T_0 = 300$  K. There is experimental evidence for a decrease in the Auger coefficients at high injection levels. This effect is explained as resulting from exciton decay, which is modeled by the items  $[1 + H \exp(-n/N_0)]$  in Eqs. (9) and (10).

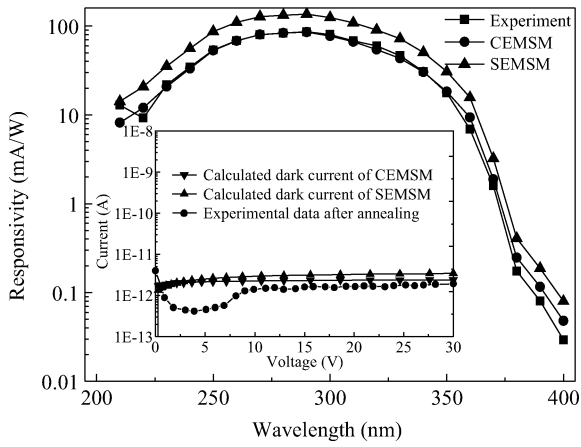


Fig. 2. Comparison of the spectral response of an SEMSM detector and a CEMSM detector with the experimental data taken from Ref. [13]. The inset shows the calculated and measured dark current characteristics<sup>[13]</sup>.

### 3. Results and discussion

#### 3.1. Verification of the numerical model

With the above established model, we calculated the responsivity and dark current characteristics of the SEMSM and CEMSM photodetectors. For the purpose of comparison, the experimental results based on the CEMSM structure are shown in Fig. 2. Excellent agreement is achieved in almost all regions of the simulated and measured spectral response of the CEMSM detector at 10 V bias. The inset in Fig. 2 shows that the calculated dark current of CEMSM is consistent with the experimental data, especially when the applied voltage is higher than 10 V. For a bias voltage lower than 10 V, the measured dark current is somewhat lower than the simulated result due to the idealized model in our calculation. Nonetheless, a general agreement between the numerical and experimental results indicates that the models used in this study are appropriate.

Under the same conditions, the spectral response and dark current characteristics of the SEMSM photodetector are also plotted in Fig. 2 for the purpose of comparison. It is clear that the overall responsivity of the SEMSM detector is enhanced. For the CEMSM structure, the UV light may normally be blocked by the metal contact on a perpendicular path. In contrast, a semicircular contact can redirect the incidence path and force excess UV light to focus on the photosensitive area. Hence, better spectral response is achieved as expected. Additionally, the SEMSM and CEMSM detectors achieve a dark current around 3 pA at a bias of 30 V. The similar dark current features of the two detectors are mainly due to the same Schottky contact area. Therefore, the SEMSM detector exhibits superiority over the conventional one by possessing high responsivity without increasing the dark current. In fact, structural parameters such as finger radius and spacing of the SEMSM detector greatly affect device performance. To obtain the optimal device performance, optimization of these parameters is indispensable.

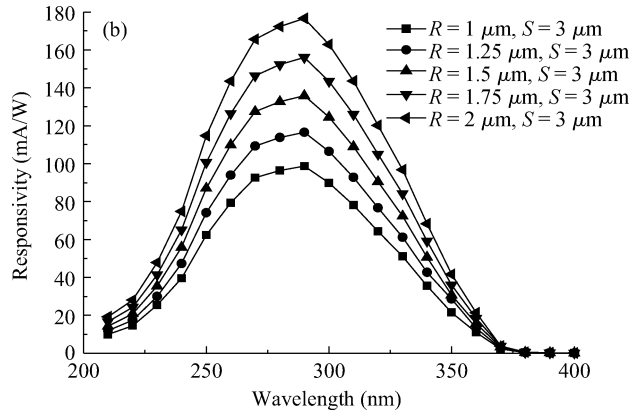
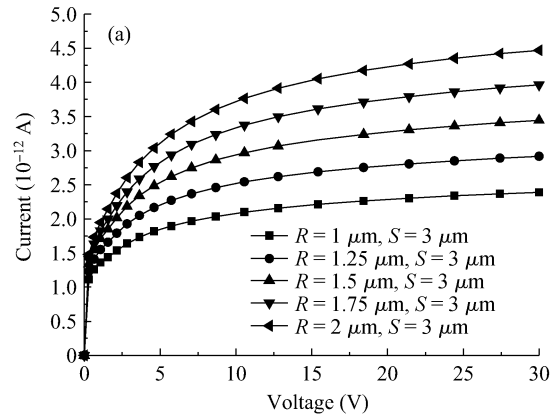


Fig. 3. (a) Dark current and (b) spectral response characteristics of the 4H-SiC SEMSM detectors with a 3  $\mu\text{m}$  electrode spacing and diverse electrode radii.

#### 3.2. The dependence of the dark current and spectral response characteristics on the contact radius

Figure 3 shows the influences of different electrode radii on the dark current and responsivity of the SEMSM detector. As is clearly visible in Fig. 3(a), dark current increases steeply when the bias is less than 10 V. Under a bias of 10 V, the dark current increases from 2.098 to 3.765 pA with an increase in the finger radius from 1 to 2  $\mu\text{m}$ . After the first rapid rise, the dark current increases slowly with the increasing voltage, and does not completely saturate at 30 V applied bias. The obvious changes in dark current can be attributed to the increased contact radius and hence the electrode area, as expected. Moreover, with the consideration of the Schottky barrier lowering model, the unsaturated dark current at higher voltages can be explained by charge accumulation at surface states and image force lowering at the edges of the electrodes<sup>[23]</sup>. The spectral response versus wavelength is plotted in Fig. 3(b) as a function of electrode radius. As is shown, it is observed that all spectral response is enhanced with the increase in contact radius. From the spectrum, we can see that the distinct spectral responsivity peak is formed at 290 nm. Similar results are observed in Ref. [13]. It is also clear that the maximum responsivity increases evidently from 0.099 to 0.177 A/W when the electrode radius increases from 1 to 2  $\mu\text{m}$ . For all response curves, the responsivity at wavelengths less than 290 nm increases rapidly. No abrupt spectral cutoff can be observed due to the fact that 4H-SiC is an indirect semiconductor and does not have a sharp

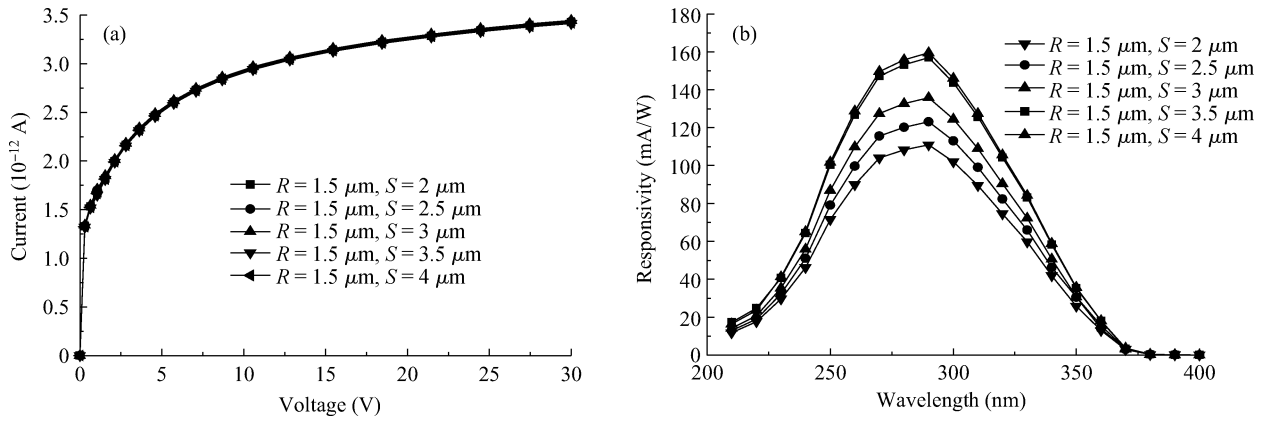


Fig. 4. The influences of various electrode spacings on (a) dark current and (b) response features with a finger width of 3  $\mu\text{m}$ .

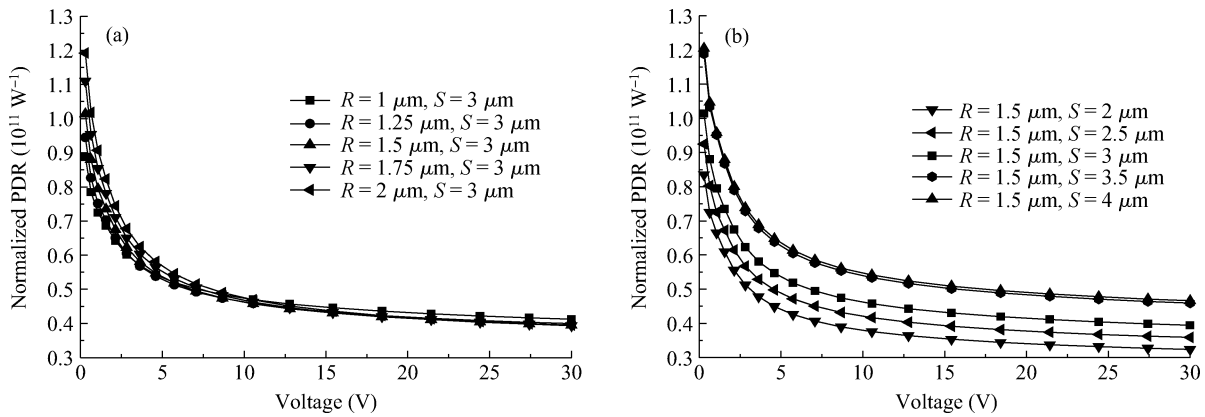


Fig. 5. Normalized ratio of photocurrent to dark current calculated (a) with various contact radii and (b) with diverse finger spacings.

cutoff edge at the band edge. The cutoff at higher wavelengths is about 380 nm, at which point the responsivity drops, largely due to moving below the bandgap of 4H-SiC. In particular, the effect of contact radius on spectral response is mainly dependent on the changes in the UV reflection area in the surface of the semicircular contacts and the vertical distribution of the electric field, which can account for the enhanced responsivity in Fig. 3(b).

**3.3. The dependence of dark current and spectral response performance on contact spacing**

The characteristics of dark current and photoresponse versus contact spacing are illustrated in Fig. 4. By adjusting the values of finger spacing from 2 to 4  $\mu\text{m}$ , it is found that the dark current of the detectors remains at the same pA level. Specifically, the dark current of these devices is below 3 pA at a bias of 10 V, and remains below 3.5 pA with the increasing applied voltage up to 30 V. The obvious differences in the dark current features, shown in Figs. 3(a) and 4(a), can be attributed to the fact that the dark current is proportional to the electrode area, which is consistent with the thermionic emission mechanism. Therefore, the effects of electrode spacing on the dark current characteristics are limited. Figure 4(b) shows the influences of diverse contact spacings on the spectral response of the detector. It is obvious that the responsivity increases with the increasing spacing. At a wavelength of 290 nm, the maximum spectral responsivity reaches 0.16 A/W, lower than the

0.177 A/W in Fig. 3(b). Furthermore, the distributions of spectral response versus contact spacing are not uniform, as compared with that of the influence of metal width on responsivity. Interestingly, with the spacing larger than 3  $\mu\text{m}$ , the responsivity appears to be relatively independent of contact spacing. For the metal spacing less than 3  $\mu\text{m}$ , not only is the curves similar to that in Fig. 3(b), but the overall responsivity is enhanced promptly as the spacing increases. The observed contact spacing dependence can be explained as follows. As the UV light illuminates the photosensitive area, most of the incident photon flux will penetrate through the active region and have high efficiency to produce the photon-generated carriers. Meanwhile, these carriers are separated and swept promptly between the contact electrodes before recombination. Photocurrent is then generated. With the increase in contact spacing ranging from 2 to 3  $\mu\text{m}$ , the active area increases and more UV beams impinge on it, which can account for the enhanced responsivity. When the spacing increases from 3.5 to 4  $\mu\text{m}$ , the increased photosensitive area is enough to absorb UV light. As a result, a detector with 4  $\mu\text{m}$  spacing exhibits a slightly improved spectral response than that of 3.5  $\mu\text{m}$ , indicating that no salient variation of responsivity can be observed.

**3.4. Optimization**

Now that we have investigated the dark current and spectral response characteristics of the SEMSM detector, the essential feature of photocurrent to dark current ratio (PDR) is criti-

cal to evaluate the performance. Nevertheless, photocurrent is directly dependent on the input optical power. Hence, normalized PDR (NPDR) is often quoted for performance assessment due to its acknowledged objectivity. NPDR can be defined as:

$$\text{NPDR} = (I_{\text{photo}}/I_{\text{dark}})/P_{\text{opt}} = (I_{\text{photo}}/P_{\text{opt}})/I_{\text{dark}} = R/I_{\text{dark}}, \quad (11)$$

where  $R$  is the responsivity in A/W. Based on the equation above, the NPDR can be calculated for various electrode radii and spacings. For different device structures, the extracted NPDR acting as a function of applied voltage at a peak wavelength of 290 nm is illustrated in Figs. 5(a) and 5(b), respectively. Clearly, both curves exhibit a decreasing tendency when the applied voltage increases to 30 V. The fact that the dark current increases with increasing bias can be responsible for the phenomenon. The different distributions of NPDR in Fig. 5 are due to various features, including photocurrent and responsivity, caused by diverse geometry sizes. Figure 5(a) shows the calculated NPDR values with different electrode radii. The curves arrange compactly and decrease gradually with increasing applied bias. Under a bias of 0.3 V, the values of NPDR are  $1.192 \times 10^{11}$ ,  $1.110 \times 10^{11}$ ,  $1.014 \times 10^{11}$ ,  $9.444 \times 10^{11}$  and  $8.875 \times 10^{11} \text{ W}^{-1}$ , respectively, with a decrease in finger radius ranging from 2 to 1  $\mu\text{m}$ . The impact of various electrode spacings on NPDR is plotted in Fig. 5(b). It is found that these curves decay distinctly as the spacing increases from 2 to 3  $\mu\text{m}$ . For  $S > 3 \mu\text{m}$ , the NPDR is independent of contact spacing and the two curves exhibit a similar trend. A detector with a 1.5  $\mu\text{m}$  finger radius and 4  $\mu\text{m}$  contact spacing possesses the maximum and the minimum NPDR of  $1.205 \times 10^{11}$  and  $4.664 \times 10^{10} \text{ W}^{-1}$  at the applied bias of 0.3 and 30 V, respectively. As is apparent in Figs. 5(a) and 5(b), we can clearly see that the top curves are comparable. For a bias lower than 5 V, no obvious changes can be found in both curves. Then, at a voltage larger than 5 V, the NPDR curve of a detector ( $R = 2 \mu\text{m}$ ,  $S = 3 \mu\text{m}$ ) decreases slightly than the top one in Fig. 5(b). The two curves present an approximate similarity but with different working mechanisms. For increasing the electrode spacing, the photosensitive area increases directly. Under UV illumination, more photo-generated carriers are produced and collected between the metal fingers. Therefore, high spectral response is achieved without fluctuating the dark current of the device, as seen in Fig. 4(a). However, a longer response time is unavoidable due to the increase in electrode spacing. On the other hand, the theoretical investigations point out that the reflection area of the electrode surface depends on the increasing contact radius, which can be responsible for the enhancement in responsivity<sup>[12]</sup>. With the fixed contact spacing, we can adjust the semicircular finger radius to improve the spectral response without reducing response speed. Nevertheless, the larger dark current caused by the increasing electrode radius may lead to a degradation in noise characteristics. Hence, the electrode radius and spacing is a contradiction affecting the features of the device. These two factors should be considered comprehensively in order to pursue a tradeoff in terms of high responsivity, low dark current and comparable NRPD. From a design point of view, the structure parameter of  $R = 2 \mu\text{m}$ ,  $S = 3 \mu\text{m}$  for an SEMSM detector is the optimal choice. Compared with the maximum spectral response of 0.16 A/W in Fig. 4(b), the detector with such a structure achieves a peak responsivity

increase of 10.7% at 290 nm.

## 4. Conclusions

In this work, we quantitatively demonstrated, for the first time, the enhanced performance of the SEMSM detector by a 2D device modeling package, ISE-DESSIS. The simulation results show that the SEMSM device has higher responsivity and a similar dark current, as compared with the conventional detector. An optimization of the SEMSM photodetector is then carried out by taking various contact radii and spacings into account. The findings indicate that a detector with a 2  $\mu\text{m}$  finger radius and 3  $\mu\text{m}$  spacing possesses comparable NRPD at 0.3 V, peak responsivity and external quantum efficiency at 290 nm of  $1.192 \times 10^{11} \text{ W}^{-1}$ , 0.177 A/W and 75.7%, respectively.

## References

- [1] Yang W F, Zhang F, Liu Z G, et al. High responsivity 4H-SiC based metal–semiconductor–metal ultraviolet photodetectors. *Sci Chin G*, 2008, 51(11): 1616
- [2] Cha H Y, Soloviev S, Zelakiewicz S, et al. Temperature dependent characteristics of nonreach-through 4H-SiC separate absorption and multiplication APDs for UV detection. *IEEE Sensors J*, 2008, 8(3): 233
- [3] Wright N G, Horsfall A B. SiC sensors: a review. *J Phys D*, 2007, 40: 6345
- [4] Zou Z Y, Yang M H, Liu T, et al. A solar-blind AlGaN-based p–i–n back-illuminated photodetector with a high temperature AlN template layer. *Journal of Semiconductors*, 2008, 29(1): 20
- [5] Li Y Y, Cheng C W, Dong X, et al. Facile fabrication of UV photodetectors based on ZnO nanorod networks across trenced electrodes. *Journal of Semiconductors*, 2009, 30(6): 063004
- [6] Su S C, Yang X D, Hu C D. Fabrication of ZnO nanowall-network ultraviolet photodetector on Si substrates. *Journal of Semiconductors*, 2011, 32(7): 074008
- [7] Lee K H, Chang P C, Chang S J, et al. GaN MSM photodetectors with an unactivated Mg-doped GaN cap layer and sputtered ITO electrodes. *J Electrochem Soc*, 2008, 155(6): J165
- [8] Narottam D, Ayman K, Mikhail V, et al. Analysis of nano-grating-assisted light absorption enhancement in metal–semiconductor–metal photodetectors patterned using focused ion-beam lithography. *Opt Commun*, 2011, 284(6): 1694
- [9] Seabra A C, Araes F G, Romero M A, et al. Increasing the optical coupling efficiency of planar photodetectors: electron beam writing of an integrated microlens array on top of a MSM device. *Proc SPIE Int Soc Opt Eng*, 2000, 4089: 890
- [10] Zhang F, Yang W F, Huang H L, et al. High-performance 4H-SiC based metal–semiconductor–metal ultraviolet photodetectors with Al<sub>2</sub>O<sub>3</sub> SiO<sub>2</sub> films. *Appl Phys Lett*, 2008, 92: 251102
- [11] Nigam S, Kim J, Luo B, et al. Effect of contact geometry on 4H-SiC rectifiers with junction termination extension. *Solid-State Electron*, 2003, 47(1): 57
- [12] Lü H M, Chen G D, Yuan J S. The relation between the electrode shape and the sensitivity of photoconductive ultraviolet detectors. *Acta Photonica Sin*, 2006, 35(7): 1052
- [13] Yang W F, Zhang F, Liu Z G, et al. Effects of annealing on the performance of 4H-SiC metal–semiconductor–metal ultraviolet photodetectors. *Mater Sci Semicond Process*, 2008, 11(2): 59
- [14] Sridhara S G, Devaty R P, Choyke W J. Absorption coefficient of 4H silicon carbide from 3900 to 3250 Å. *J Appl Phys*, 1998, 84(5): 2963

- [15] Su Y K, Chang S J, Chen C H, et al. GaN metal–semiconductor–metal ultraviolet sensors with various contact electrodes. *IEEE Sensors J*, 2002, 2(4): 366
- [16] DESSIS-ISE, 2D Semiconductor Device Simulator version 10.0 2005 Integrated Systems Engineering, Zurich
- [17] Chen B, Yang Y T, Li Y J, et al. Simulation and optimization of a 6H-SiC metal–semiconductor–metal ultraviolet photodetector. *Journal of Semiconductors*, 2010, 31(6): 064010
- [18] Matsuura H. Influence of excited states of deep acceptors on hole concentrations in SiC. *Mater Sci Forum*, 2002, 389–393: 679
- [19] Yu Y P, Cardona M. *Fundamentals of semiconductors: physics and materials properties*. Chapter 4. 2nd ed. Berlin Springer, 1999
- [20] Brennan K F. *The physics of semiconductors with application to optoelectronic devices*. Chapter 5. Cambridge: Cambridge University Press, 1999
- [21] Galeckas A, Linnros J, Grivickas V, et al. Auger recombination in 4H-SiC: unusual temperature behavior. *Appl Phys Lett*, 1997, 71(22): 3269
- [22] Neimontas K, Aleksiejunas R, Sudzius M, et al. Optical studies of nonequilibrium carrier dynamics in highly excited 4H-SiC epitaxial layers. *Mater Sci Forum*, 2005, 483–485: 413
- [23] Sabuktagin S, Moon Y T, Dogan S, et al. Observation of surface charging at the edge of a Schottky contact. *IEEE Electron Device Lett*, 2006, 27(4): 211